Analysis of Mapping Coverage Obtained from Spacecraft

Anastassios E. Petropoulos*and James M. Longuski†
Purdue University, West Lafayette, Indiana 47907-1282

An exact analysis of the coverage obtained by spacecraft using cross-track scanning and nadir-centered conical imaging, under imposed viewing obliqueness and resolution requirements, is presented. In addition to exact expressions for the area acquired and the area acquisition rate, envelope theory is introduced to obtain the boundary of the imaged area. These expressions are relatively compact, allowing rapid machine computation. The effects of the sun phase angle, and of imaging system limitations are also examined. The Galileo mission encounter with Callisto is used as a numerical example, from which certain general conclusions are drawn regarding optimal imaging trajectories.

1. Introduction

One of the major goals in the exploration of the solar system is to map and image the surfaces of the planets and their satellites. In spite of this fact, there is a dearth of exact analytic methods for assessing the mapping coverage obtained by spacecraft during flybys or in closed orbits. This paper analyzes the coverage problem for two common imaging techniques (see Pease[1] and Slater[2]) and two different types of mapping requirements. In all cases the mapped body is modelled as a sphere, and the spacecraft is assumed to be on a conic trajectory, with the equator of the sphere taken as the orbital plane.

The first technique considered is meridional cross-track scanning, where the optics continually scan a thin column of area perpendicular to the spacecraft groundtrack. Cross-track scanning is usually accomplished by a pushbroom, whiskbroom or raster scan method. The second technique is nadir-centered conical scanning, in which the area acquired is a spherical cap centered on the nadir. This type of imaging can be effected either by a simple camera and lens which would provide a viewing cone with vertex at the spacecraft, or by panning the instrument instantaneous field of view appropriately. For the purposes of this analysis, these scanning methods are idealized as providing instantaneous area acquisition, which in practice means that the optics can operate sufficiently quickly so that the instrument footprint is not distorted by the spacecraft motion. The footprint geometries are shown in Figure 1.

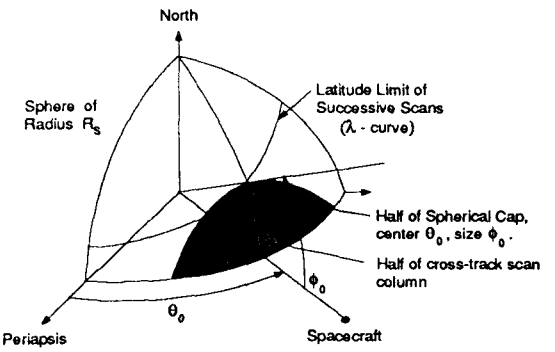

Fig. 1. Conical and cross-track scanning geometries.

Viewing obliqueness and resolution will be examined individually as mapping requirements. As described by Longuski and Myers,[3] the Galileo mission eliminated highly oblique images from consideration, since they were of no scientific value. However, if the resolution is sufficiently good (for example, due to high resolution optics, or due to proximity), even oblique images can be considered. Thus, each of the mapping requirements will impose a latitude limit, or λ-*curve*, beyond which the requirements will no longer be met; *i.e.*, the images will be too oblique, or, for the resolution limited case, the resolution will be too poor. It will be assumed that the optical system is capable of imaging at least up to the latitude limit.

In Longuski and Myers,[3] where only obliqueness constrained viewing is considered, an integral is presented for the area seen by cross-track imaging (that is, the area under the obliqueness limited λ-curve),

*Graduate Student, School of Aeronautics and Astronautics; currently Developer, Cambridge Technology Partners, Suite 111, 222 N. Washington Square, Lansing, MI 48933. AIAA Student Member.

†Associate Professor, School of Aeronautics and Astronautics. Associate Fellow AIAA. Member AAS.

which is then accurately approximated by considering only the first eight terms of the integrand's series expansion. The following section of the present paper shall provide a general infinite series representation of this integral. A similar integral for resolution limited viewing is provided in terms of a quadrature based on the resolution limited λ-curve computed in the fourth section of the paper. The third section will develop a theory of envelopes generalized from Boltyanskii,[4] which is then applied in the fourth section to determine parametrically the boundary (or "envelope") of area imaged by conical viewing under both types of mapping requirements. The fifth section will provide a compact, explicit expression for the rate at which new area is acquired in conical scanning, which can be numerically integrated to obtain the total area imaged. Both the envelope and area rate analyses are general and can be applied to conical scanning with any sort of mapping requirement. The sixth section deals with sun illumination requirements for viewing and with camera losses. A numerical example based on the Galileo project is then considered in the last section.

2. Cross-Track Emission Angle Limited Imaging

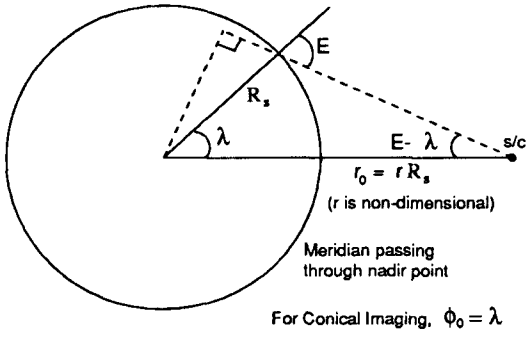

Fig. 2. The emission angle constraint.

The emission angle, E, at a point on the planet is defined as the angle between the line of sight to the spacecraft and the local vertical, as shown in Figure 2. To prevent extremely oblique viewing, the maximum value of the emission angle is constrained, for example to $E = 60°$ (the limit accepted by the Galileo mission, Longuski and Myers[3]), which then determines the latitude limit,

$$\begin{aligned} r_0 \sin(E - \lambda) &= R_s \sin E \\ \lambda &= E - \sin^{-1}[(\sin E)/r] . \end{aligned} \quad (1)$$

Since the width of the scanned column can be considered infinitesimal compared to its height, the imaged

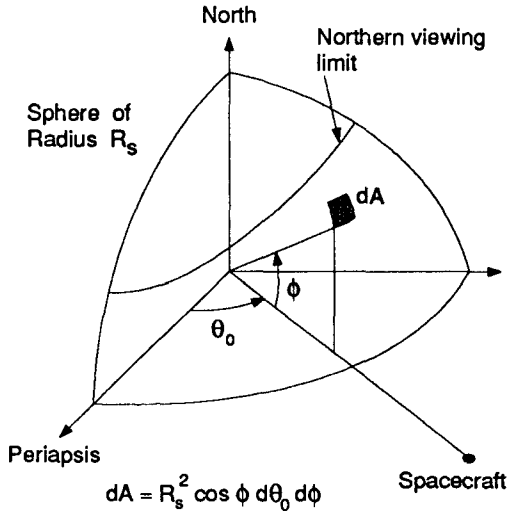

Fig. 3. Spherical geometry of the observable area.

area can be obtained by direct integration under the λ-curve. Using the spherical geometry of Figure 3 and assuming that viewing is symmetrical about the equator, the area imaged, expressed as a fraction of the total planet area, is given by the integral

$$A = \frac{1}{2\pi} \int_{\theta_i}^{\theta_f} \int_0^{\lambda} \cos\phi \, d\phi \, d\theta_0 = \frac{1}{2\pi} \int_{\theta_i}^{\theta_f} \sin\lambda \, d\theta_0 . \quad (2)$$

Substituting for λ from Equation (1),

$$A = \frac{1}{2\pi} \int_{\theta_i}^{\theta_f} \left(-\frac{cosE \sin E}{r} + \sin E \sqrt{1 - \frac{\sin^2 E}{r^2}} \right) d\theta_0 . \quad (3)$$

Two integrals result from Equation (3),

$$J = \int_{\theta_i}^{\theta_f} \frac{1 + e\cos\theta_0}{p} \, d\theta_0 = \frac{1}{p} [I_0 + e(\sin\theta_f - \sin\theta_i)] \quad (4)$$

$$I = \int_{\theta_i}^{\theta_f} \sqrt{1 - \frac{\sin^2 E}{r^2}} \, d\theta_0 , \quad (5)$$

where the conic equation $r = p/(1+e\cos\theta_0)$ has been used in the first integral with

$$I_0 = \theta_f - \theta_i . \quad (6)$$

The remainder of this section presents an evaluation of the second integral in series form. Although several changes of integration variable were considered, it was found easiest to use θ_0. Since $[(\sin E)/r]^2 < 1$, the square root term can be written in a binomial expansion which has the general form,

for $|x| < 1$,

$$(1-x)^{\frac{1}{2}} = 1 - \sum_{k=1}^{k=\infty} b_1(k) x^k,$$

where

$$b_1(k) = \begin{cases} \frac{1}{2} & \text{if } k = 1 \\ \dfrac{(2k-3)!}{2^{2k-2} k!(k-2)!} & \text{if } k = 2,3,4,\ldots \end{cases} . \tag{7}$$

Equation (5) thus takes on the series form

$$I = \int_{\theta_i}^{\theta_f} d\theta_0 - \sum_{k=1}^{k=\infty} b_1(k) I_k \,, \tag{8}$$

where

$$\begin{aligned} I_k &= \sin^{2k} E \int_{\theta_i}^{\theta_f} r^{-2k}\, d\theta_0 \\ &= \left(\frac{\sin E}{p}\right)^{2k} \int_{\theta_i}^{\theta_f} (1 + e\cos\theta_0)^{2k}\, d\theta_0 \,. \end{aligned}$$

I_k is now evaluated by expanding the integrand into a sum of $2k+1$ terms and integrating each individually.

$$\begin{aligned} I_k &= \left(\frac{\sin E}{p}\right)^{2k} \int_{\theta_i}^{\theta_f} \sum_{n=0}^{2k} \binom{2k}{n} e^n \cos^n\theta_0\, d\theta_0 \\ &= \left(\frac{\sin E}{p}\right)^{2k} \sum_{n=0}^{2k} \binom{2k}{n} e^n \int_{\theta_i}^{\theta_f} \cos^n\theta_0\, d\theta_0 \\ &= \left(\frac{\sin E}{p}\right)^{2k} I_0 + \left(\frac{\sin E}{p}\right)^{2k} \sum_{n=1}^{2k} \binom{2k}{n} e^n \sin\theta_0 \\ &\quad \times \begin{cases} \left[\sum_{s=0}^{\frac{n-1}{2}} \frac{2^{n-1-2s}\left(\frac{n-1}{2}!\right)^2 (2s)!}{n!(s!)^2} \cos^{2s}\theta_0\right]_{\theta_i}^{\theta_f}, & n \text{ odd} \\ \left[\sum_{s=0}^{\frac{n}{2}-1} \frac{n!(s!)^2}{2^{n-2s}(2s+1)!\left(\frac{n}{2}!\right)^2} \cos^{2s+1}\theta_0 \right. \\ \qquad \left. + \frac{n!}{2^n\left(\frac{n}{2}!\right)^2}\theta_0\right]_{\theta_i}^{\theta_f}, & n \text{ even} \end{cases} \end{aligned}$$

where the standard definition of the binomial coefficient has been used,

$$\binom{2k}{n} = \frac{(2k)!}{n!(2k-n)!} \,.$$

As it is unwieldy having the distinction between n odd and n even, n is allowed to run from 1 to k in the outer sum, and is therefore replaced by $2n-1$ in the odd case and $2n$ in the even case. In addition, the relationship $p = r_p(1+e)$ is used, resulting in

$$\begin{aligned} I_k = \left(\frac{\sin E}{r_p}\right)^{2k} \Bigg(&\sum_{n=0}^{k} b_2(k,n) \frac{e^{2n}}{(1+e)^{2k}} I_0 \\ &+ \sum_{n=1}^{k} \sum_{s=0}^{n-1} \Bigg[\sin\theta_0 \frac{e^{2n-1}}{(1+e)^{2k}} \{ c_1(k,n,s)\cos^{2s}\theta_0 \\ &+ e\, c_2(k,n,s)\cos^{2s+1}\theta_0 \} \Bigg]_{\theta_i}^{\theta_f} \Bigg) , \end{aligned} \tag{9}$$

where

$$b_2(k,n) = \binom{2k}{n} \frac{(2n)!}{2^{2n}(n!)^2} = \frac{(2k)!}{2^{2n}(n!)^2(2k-2n)!} \tag{10}$$

$$c_1(k,n,s) = \binom{2k}{2n-1} \frac{2^{2n-2-2s}((n-1)!)^2(2s)!}{(2n-1)!(s!)^2} \tag{11}$$

$$\begin{aligned} c_2(k,n,s) &= \binom{2k}{2n} \frac{(2n)!(s!)^2}{2^{2n-2s}(2s+1)!(n!)^2} \\ &= \frac{(2k)!(s!)^2}{2^{2n-2s}(2k-2n)!(2s+1)!(n!)^2} \,. \end{aligned} \tag{12}$$

Thus, the integral I of Equation (5) has been represented as an infinite sum of integrals, I_k, as shown in Equation (8). In Equation (9), the I_k have in turn been evaluated as a finite double sum. These series, together with the trivially evaluated integral J of Equation (4), and the definitions of the four coefficients in Equations (7) and (10) - (12), allow us to evaluate the area in Equation (3):

$$A = (2\pi)^{-1}(I - J\cos E)\,\sin E.$$

The rate of convergence of the series is determined primarily by the quantity $[(\sin E)/r_p]^{2k}$, which multiplies the double sum of Equation (9) and decreases rapidly with k (as long as the trajectory is not subsurface), thereby off-setting the increase with k in the number of terms in the sum. Various numerical evaluations of the series expression for A have been made, all showing convergence. The value of k where the contribution of I_k to the series form of I, in Equation (8), dropped below 10^{-6} was found to range between 20 and 4, for $r_p = 10/9$ to 10, $e = 1$ to 10, and $E = 60°$. Computation of the area by direct numerical integration for a number of sample cases demonstrates agreement within the tolerance limits of the integration with the area computed using the series above.

3. Envelope Theory

In cross-track imaging, successive footprints do not overlap, allowing them to be added up directly

by integration to give the total imaged area. However, in the case of conical imaging the overlap area is non-zero and this necessitates some other method of determining the imaged area and its envelope. This section presents a general method by which envelopes can be computed.

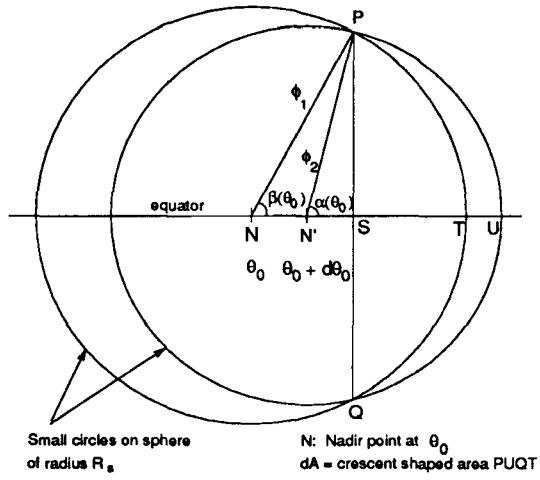

Fig. 4. Generation of the envelope and geometry of the differential area segment.

Conical scanning provides a good vehicle for explaining the envelope concept. The boundary of the footprint is a small circle on the sphere. As the spacecraft moves, the size and location of the circle both change (see Figure 4) and may be considered as parameters. If these parameters vary smoothly, and in such a way as to avoid engulfing of one circle by another, then it will be possible to find a curve, the envelope curve, which is tangent to all of the small circles. Clearly this tangent curve provides a boundary for all area that has been passed over by the circles. It is not without merit, then, that the tangent curve be named the envelope, while the small circle, whose size and location vary, is called the generating curve. As for the determination of this envelope, one need only note that the closer together two circles are, the closer is their intersection point to the points of tangency of the envelope with each of the two circles. In the limit, these three points coalesce into one. Thus the task of finding the envelope is reduced to finding the set of all intersection points of infinitesimally close circles.

To generalize, let us move into $\mathcal{R}^n$, where the generating curve will, in general, be a surface, as will be the envelope. Let the generating surface depend on m parameters, which, for convenience, shall be considered as the components of a parameter vector, $\vec{\alpha}$. Let the generating *surface equation* be

$$f(\vec{x}, \vec{\alpha}) = 0, \qquad \text{where } \vec{x} \in \mathcal{R}^n,\ \vec{\alpha} \in \mathcal{R}^m. \tag{13}$$

Since we wish the envelope to be a surface and not a volume, there must be $m-1$ constraint equations on the parameters. This effectively means that the generating surface varies with only one parameter, although this parameter is not necessarily expressible explicitly in terms of the known components of the parameter vector. Were this not the case, the movement of the generating surface would not be sufficiently constrained and the set of intersection points would occupy a volume. This is easily exemplified by slightly altering the scanning circles, above, and considering them to lie on a two-dimensional plane instead of on a sphere. If the size and location of the circles could vary independently, then the circles (and the intersection points of infinitesimally close pairs) would cover the whole plane. Thus, the envelope, which is the set of these intersection points, is the whole plane. In $\mathcal{R}^n$ this plane would be a volume. Therefore we apply the following *constraint equations*

$$g_i(\vec{\alpha}) = 0, \qquad i = 1, 2, \ldots, m-1. \tag{14}$$

These equations describe surfaces in the parametric space, $\mathcal{R}^m$. Turning now to the generating surface, the envelope is given by the intersection points of the surface $f(\vec{x}, \vec{\alpha}) = 0$ and the neighboring surface $f(\vec{x}, \vec{\alpha} + d\vec{\alpha}) = 0$, where $d\vec{\alpha}$ is an infinitesimal change in the parameter vector. With this perspective, the generating surface can be considered a surface in the parametric space, dependent on $\vec{x}$. The infinitesimal vector, $d\vec{\alpha}$, must be tangential to this surface, since the points $\vec{\alpha}$ and $\vec{\alpha} + d\vec{\alpha}$ both lie on it. In other words, $d\vec{\alpha}$ must be orthogonal to the gradient of f with respect to $\vec{\alpha}$, denoted $\nabla_\alpha f$. The same must be true for the constraining surfaces $g_i(\vec{\alpha}) = 0$. With the definition

$$\nabla_\alpha = \left[\frac{\partial}{\partial \alpha_1} \quad \cdots \quad \frac{\partial}{\partial \alpha_m}\right],$$

the orthogonality conditions can be expressed as

$$\nabla_\alpha f(\vec{x}, \vec{\alpha}) \,.\, d\vec{\alpha} = 0$$

$$\nabla_\alpha g_i(\vec{\alpha}) \,.\, d\vec{\alpha} = 0, \qquad i = 1, 2, \ldots, m-1.$$

Since $d\vec{\alpha} \neq 0$ (it is infinitesimal, but not zero), the matrix whose rows are taken as the above gradients must be singular. In other words, there is a *determi-*

nant equation

$$\begin{vmatrix} \frac{\partial f}{\partial \alpha_1} & \cdots & \frac{\partial f}{\partial \alpha_m} \\ \frac{\partial g_1}{\partial \alpha_1} & \cdots & \frac{\partial g_1}{\partial \alpha_m} \\ \vdots & & \vdots \\ \frac{\partial g_{m-1}}{\partial \alpha_1} & \cdots & \frac{\partial g_{m-1}}{\partial \alpha_m} \end{vmatrix} = 0. \qquad (15)$$

Equations (13)-(15) are $m+1$ equations in m unknowns, namely the parameters α_i. The envelope is then the solution set in $\vec{x}$ of these equations. The α_i cannot always be entirely eliminated, in which case the envelope must remain implicitly defined. In the next section, the envelope will be determined for the general nadir-centered conical scanning case, in which the size of the imaged circle has an arbitrary functional dependence on the location of the circle.

4. General Nadir-Centered Conical Envelope and Resolution Limited Imaging

Let the size of the imaged circle be given by the half-angle, denoted ϕ_0, subtended at the center of the sphere by two diametrically opposed points on the circle. The location of the circle will be given by the longitude of its center point. Assuming nadir-centered viewing, this longitude is equal to the true anomaly, θ_0, of the spacecraft. The latitude of the nadir point is of course zero, by our definition of the equatorial plane. To apply the envelope theory, it is necessary to find one constraint equation relating ϕ_0 and θ_0.

Fortunately, for both the emission angle limited and the resolution limited viewing cases, ϕ_0 can be found as an explicit function of θ_0. In effect, this makes the surface equation dependent on only one parameter, thereby eliminating the need for any constraint equation. It is convenient, however, to retain ϕ_0 as an auxiliary parameter. In the E-limited viewing case, the circle size is given by λ in Equation (1), which, in conjunction with the conic equation, yields

$$\phi_0(\theta_0) = E - \sin^{-1}\left[\frac{1+e\cos\theta_0}{r_p(1+e)}\sin E\right]. \qquad (16)$$

4.1. Resolution Limited Imaging

Before applying the envelope theory, let us also determine the resolution limited circle size. In Figure 5, let D be the required linear mapping resolution. That is, the physical separation of any two barely distinguishable points on the map must be at most equal

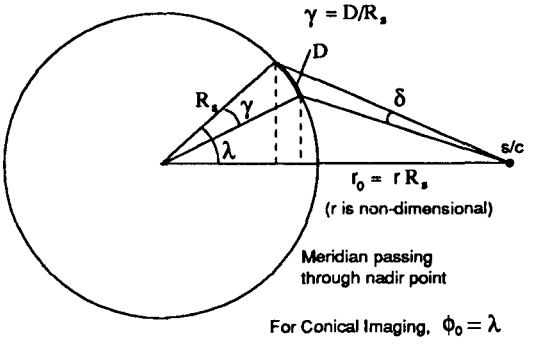

Fig. 5. The resolution constraint.

to D. This permits the definition of the required angular mapping resolution as $\gamma = D/R_s$. The angular resolution of the optical system, denoted δ, shall be taken to be the angular separation at the viewing apparatus of two barely distinguishable points. Given γ and δ, we must now determine how the imaged circle size depends on r. Clearly the resolution obtained deteriorates as one moves away from the nadir. Moreover, at any non-nadir point, the resolution is poorest when moving directly away from the nadir on a great circle through the nadir point. Thus, in Figure 5 we look at the resolution along a meridian, and determine the latitude where the resolution becomes worse than γ. In practice, the two barely distinguishable points always lie in the same hemisphere, which means that $0 < \gamma + \delta < \pi/2$. Thus, although this constraint is not theoretically imposed, it is assumed nevertheless.

With reference to Figure 5, one finds

$$\delta = \tan^{-1}\left(\frac{\sin\phi_0}{r-\cos\phi_0}\right) - \tan^{-1}\left[\frac{\sin(\phi_0-\gamma)}{r-\cos(\phi_0-\gamma)}\right].$$

After some trigonometric manipulation, the following unexpectedly compact result is obtained for the size of the imaged circle:

$$\phi_0(r) = \frac{\gamma}{2} + \cos^{-1}\left[\frac{r^2\tan\delta + (\sin\gamma + \cos\gamma\tan\delta)}{2r(\sin\frac{\gamma}{2} + \cos\frac{\gamma}{2}\tan\delta)}\right] \qquad (17)$$

or

$$\phi_0(\theta_0) = \frac{\gamma}{2} + \cos^{-1}\left\{\frac{1}{2(\sin\frac{\gamma}{2}+\cos\frac{\gamma}{2}\tan\delta)}\left[\frac{r_p(1+e)\tan\delta}{1+e\cos\theta_0} + \frac{(1+e\cos\theta_0)(\sin\gamma+\cos\gamma\tan\delta)}{r_p(1+e)}\right]\right\}. \qquad (18)$$

Clearly, Equation (17) cannot apply for all values of r. For r larger than some final distance, r_f, the quantity

whose inverse cosine is taken becomes greater than unity, making the equation invalid, meaning that no area can be imaged at the required resolution beyond this distance. After some algebra and trigonometry, and a certain amount of luck, one obtains the following result for r_f by setting $\phi_0 = \gamma/2$

$$r_f = \cos\frac{\gamma}{2} + \left(\frac{1}{\tan\delta} + \frac{1}{\sin\delta}\right)\sin\frac{\gamma}{2}. \qquad (19)$$

This is just one of two solutions for r_f. The second solution is of no concern, however, since it is less than unity. For completeness, this solution is given as $r_{f_2} = \cos(\gamma/2) + (1/\tan\delta - 1/\sin\delta)\sin(\gamma/2)$.

Correspondingly, there is a lower limit for which Equation (17) is valid. Although this rarely would occur in practice (unless the resolution requirement is very poor) it is examined for purposes of thoroughness. Given γ and δ, the distance r can always be made sufficiently small, but still greater than unity (i.e. we remain outside the planet surface), such that the resolution achieved at the horizon, where the line of sight is tangential to the planet, is better than the required resolution γ. The distance, r_t, where these two resolutions are equal is found by geometry as follows

$$\begin{aligned} \tan\delta &= (1-\cos\gamma)/\sqrt{r_t^2 - 1} \\ r_t &= \left[\frac{(1-\cos\gamma)^2}{\tan^2\delta} + 1\right]^{\frac{1}{2}}. \end{aligned} \qquad (20)$$

For $r < r_t$, imaging at, or better than, the required resolution is possible all the way out to the horizon. It should be noted, however, that r_t is exceedingly close to unity for all but the poorest of resolution requirements, unless the optics have superb angular resolution. The latitude of the horizon is simply given as

$$\phi_0 = \cos^{-1} r^{-1} \qquad (21)$$

while the actual resolution obtained at the horizon is given by

$$\gamma_{hor} = \cos^{-1}\left(1 - \tan\delta\sqrt{r^2 - 1}\right).$$

This resolution at the horizon is defined so long as half or less of the planet falls within the angular resolution of the optics, i.e. up to $r = \sqrt{1/\tan^2\delta + 1}$ (a large number, even for mediocre optics).

In summary, the pertinent equations that define the size of the imaged circle as a function of distance (and hence, true anomaly) are presented below, for the various ranges of r.

$1 < r \leq r_t \Rightarrow$ resolution requirement exceeded (21).

$r_t < r \leq r_f \Rightarrow$ resolution requirement met (17).

$r_f < r < \infty \Rightarrow$ no area imaged at required resolution.

We shall be concerned only with the middle range of r in this paper. Note that Equation (18) provides the resolution limited λ-curve, which can be used with Equation (2) to obtain by quadrature the cross-track area imaged in the resolution limited case.

4.2. The Envelope

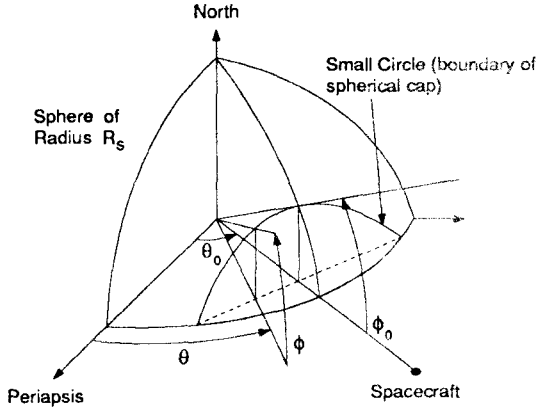

Fig. 6. Geometry for the conical imaging surface equation.

The circle size has now been established as a function of true anomaly for both the E-limited and the resolution limited viewing cases, enabling attention to be focussed on the envelope. The remaining necessary component for applying the envelope theory is the determination of the surface equation, which in this case is the equation of the small circle centered at θ_0. From the geometry of Figure 6, the surface equation is seen to be

$$\cos(\phi)\,\cos(\theta - \theta_0) = \cos[\phi_0(\theta_0)] \qquad (22)$$

Differentiating with respect to the parameter θ_0 to obtain the determinant equation,

$$\cos\phi\,\sin(\theta - \theta_0) = -\phi_0'(\theta_0)\sin[\phi_0(\theta_0)]. \qquad (23)$$

These last two equations are then solved to give parametric expressions, in terms of the true anomaly, for θ and ϕ, the longitude and latitude coordinates, respectively, of the envelope. The two equations yield the solutions

$$\theta^* = \theta_0 - \tan^{-1}(\phi_0'\tan\phi_0) \qquad (24)$$

$$\phi^* = \cos^{-1}\left(\cos\phi_0\sqrt{1 + \phi_0'^2\tan^2\phi_0}\right), \qquad (25)$$

where the asterisk denotes envelope values for longitude and latitude. The functions $\phi_0(\theta_0)$ have already been established for both the E-limited and the resolution limited case. Their derivatives are computed as follows. For the E-limited case,

$$\phi_0'(\theta_0) = \frac{e \sin\theta_0}{r_p(1+e)\cos(E-\phi_0)} \sin E \qquad (26)$$

and for the resolution limited case

$$\phi_0'(\theta_0) = \frac{e \sin\theta_0}{2\sin(\phi_0 - \frac{\gamma}{2})\cos\frac{\gamma}{2}(\tan\frac{\gamma}{2} + \tan\delta)} \times \left[\frac{\cos\gamma\,(\tan\gamma + \tan\delta)}{r_p(1+e)} - \frac{r_p(1+e)\tan\delta}{(1+e\cos\theta_0)^2}\right]. \qquad (27)$$

With the proviso that engulfing does not occur (no circle is contained entirely within previous or subsequent circles), Equations (24) and (25) establish the envelope for both types of mapping requirements with conical nadir-centered imaging. The envelope is useful in that it demarcates the area mapped. However, to actually calculate the area it is necessary to integrate under the envelope, which results in an intractable problem. Instead, spherical geometry is used to obtain a much simpler, albeit also analytically intractable, expression for the rate at which the conical scan acquires new area. This expression may then be easily integrated numerically to obtain the total area imaged.

5. Area Acquisition Rate for Conical Scanning

This section is devoted to the determination of the derivative of the area imaged with respect to the spacecraft true anomaly. The problem of engulfing is also examined. As seen in Figure 4, in the absence of engulfing, a small change, $d\theta_0$, in the true anomaly of the nadir point yields a crescent-shaped patch of area, dA, that has not been previously imaged, either in whole or in part (see Figure 9 and the associated analysis of the recounting problem).

The first step in determining the crescent-shaped area is the introduction of the appropriate great circles, namely the equator, the meridian through P and Q, the great circle through N and P, and the great circle through N' and P. This allows the differential area to be expressed as

$$dA = 2[\text{Sector } N'PU - \text{Sector } NPT + \triangle NPN'], \qquad (28)$$

where $\triangle NPN'$ is a spherical triangle since its sides are all great circles. Once again, all areas shall be expressed as fractions of the total surface area of the sphere. The area of a spherical triangle is determined by its spherical excess, $X = (\hat{N}+\hat{N}'+\hat{P}-\pi)$, in other words the amount by which the sum of the angles at the vertices exceeds π. The (non-dimensional) area is then given by $\triangle NPN' = X/(4\pi)$. The area of the sectors, meanwhile, is determined by the angles β and α. For convenience we define $\phi_1 = \phi_0(\theta_0) = \angle NP$ and $\phi_2 = \phi_0(\theta_0 + d\theta_0) = \angle N'P$, where $\angle NP$ denotes the angle subtended by the great arc NP. By applying formulas from the mensuration of spheres to $\triangle NPN'$, one obtains

$$\cos(\pi - \alpha) = \frac{\cos\phi_1 - \cos\phi_2 \cos d\theta_0}{\sin\phi_2 \sin d\theta_0} \qquad \alpha \in (0,\pi) \qquad (29)$$

$$\cos\beta = \frac{\cos\phi_2 - \cos\phi_1 \cos d\theta_0}{\sin\phi_1 \sin d\theta_0} \qquad \beta \in (0,\pi) \qquad (30)$$

$$\tan\frac{X}{4} = \sqrt{\tan\frac{s}{2}\tan\frac{1}{2}(s-\phi_1)\tan\frac{1}{2}(s-\phi_2)\tan\frac{1}{2}(s-d\theta_0)}, \qquad (31)$$

where

$$s = \frac{1}{2}(\phi_1 + \phi_2 + d\theta_0).$$

Then, from Equation (28),

$$dA = \frac{1}{2\pi}[\alpha(1-\cos\phi_2) - \beta(1-\cos\phi_1) + X]. \qquad (32)$$

Next, the Taylor expansion of $\phi_2 = \phi_0(\theta_0 + d\theta_0)$ is taken about θ_0. The result is inserted into Equations (29) - (31), and then the series expansions of α, β and X about θ_0 are computed:

$$\alpha = \cos^{-1}(-\phi_0') + \frac{1}{2}\left[\cot\phi_0\sqrt{1-\phi_0'^2} + \frac{\phi_0''}{\sqrt{1-\phi_0'^2}}\right] d\theta_0 + \mathcal{O}(d\theta_0{}^2)$$

$$\beta = \cos^{-1}(-\phi_0') - \frac{1}{2}\left[\cot\phi_0\sqrt{1-\phi_0'^2} - \frac{\phi_0''}{\sqrt{1-\phi_0'^2}}\right] d\theta_0 + \mathcal{O}(d\theta_0{}^2)$$

$$X = \frac{1-\cos\phi_0}{\sin\phi_0}\sqrt{1-\phi_0'^2}\, d\theta_0 + \mathcal{O}(d\theta_0{}^2).$$

These results are inserted into Equation (32) to obtain

$$dA = \frac{\sin\phi_0}{2\pi}\left[\phi_0'\cos^{-1}(-\phi_0') + \sqrt{1-\phi_0'^2}\right] d\theta_0 + \mathcal{O}(d\theta_0{}^2). \qquad (33)$$

In obtaining the $\mathcal{O}(d\theta_0)$ terms (terms of order $d\theta_0$) for α and β, it was necessary to take the Taylor expansion of ϕ_2 up to the $\mathcal{O}({d\theta_0}^2)$ term, as witnessed by the presence of a ϕ_0'' term. However, this term conveniently drops out of the $\mathcal{O}(d\theta_0)$ expression of dA. In the limit $d\theta_0 \to 0$, Equation (33) yields

$$\frac{dA}{d\theta_0} = \frac{\sin\phi_0}{2\pi}\left[\phi_0' \cos^{-1}(-\phi_0') + \sqrt{1-\phi_0'^2}\right] . \quad (34)$$

This derivative represents the rate with respect to true anomaly at which new area is imaged. The functions $\phi_0(\theta_0)$ and $\phi_0'(\theta_0)$ have already been computed for both the E-limited and the resolution limited cases in Equations (16), (18), (26) and (27). Considering the complicated expressions involved, Equation (34) does not appear to be analytically integrable in closed form. Thus, in order to find the *total area imaged*, one must integrate Equation (34) numerically, remembering to take into account the fact that the imaged circle at the integration starting point is not included in the integral, while the circle at the end-point is included.

5.1. Engulfing

It is clear that if the imaged circles are enlarging (or diminishing) rapidly enough, then a condition may arise where the circle imaged from the current spacecraft position contains (or is contained by) the circle obtained from the spacecraft's infinitesimally close prior position. The term *engulfing* shall be used to describe this condition, both for the enlarging and for the diminishing cases. This may also be depicted graphically. In Figure 4, we have, to first order, that $N'U = \phi_2 = \phi_1 + \phi_0' d\theta_0$. Thus, $TU = N'U - NT + d\theta_0 = \phi_0' d\theta_0 + d\theta_0$. When TU becomes negative, the circle at N' is entirely engulfed in the circle at N. This means that $\phi_0' < -1$. Similarly the circle at N' will engulf the circle at N if $\phi_0' > +1$. In brief, we have the *engulfing condition*:

$$|\phi_0'(\theta_0)| > 1 . \quad (35)$$

As expected, the area derivative of Equation (34) is undefined when engulfing occurs. Is the engulfing condition ever met? For E-limited viewing, the answer can be proved to be in the negative (at least for non-subsurface trajectories.) However, it is found numerically that engulfing does occur in resolution limited imaging. As the spacecraft approaches the planet, initially no area is visible at the required resolution. Then a tiny circle is imaged, from distance $r = r_f$. The circle grows very rapidly, engulfing the previously imaged circles ($\phi_0' > 1$). Then engulfing typically ceases until the post encounter phase, where the reverse occurs - the circle contracts so rapidly that it is engulfed in previous circles ($\phi_0' < -1$), until it finally vanishes at $r = r_f$. This sequence of imaged circles is conveniently depicted by an *igloo plot* (Figure 7), which shows the Northern hemisphere portion of the post-encounter imaged circles, along with the λ-curve and the envelope. There is, of course, North-South and East-West symmetry in the imaged area so that the total area is four times that depicted in Figure 7 (between $\theta_0 = 0°$ and $\theta_0 \approx 151°$). A similar *tunnel plot*, which never displays engulfing, is shown for the E-limited viewing case, Figure 8. Both plots conveniently depict the fact that the envelope, where it exists, is tangent to the imaged circles.

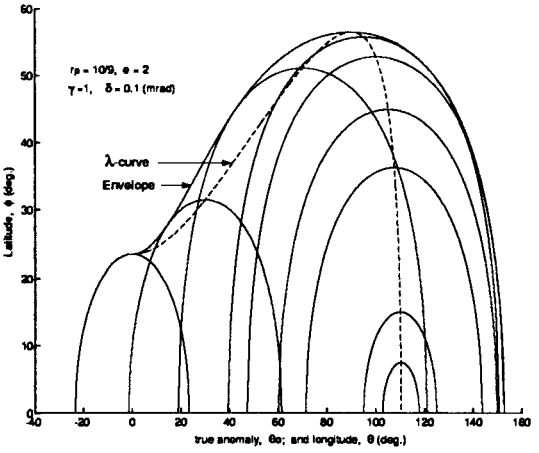

Fig. 7. Igloo plot: Imaged circles, envelope, and λ-curve for resolution limited imaging.

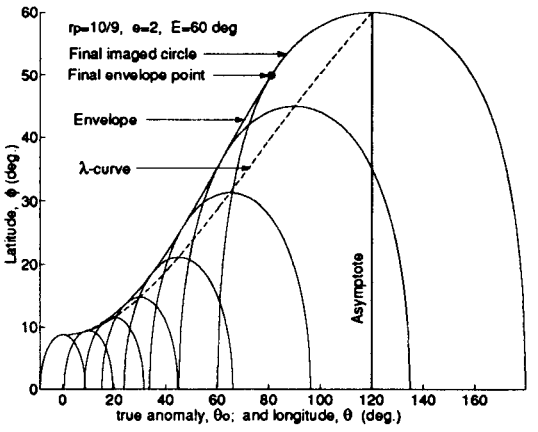

Fig. 8. Tunnel plot: Imaged circles, envelope, and λ-curve for emission angle limited imaging.

As there is no engulfing in the E-limited case, the

area can be directly obtained by integrating Equation (34). The question arises as to the computation of the area when engulfing occurs. Using the resolution limited case as an example, the area is computed by integrating Equation (34) from the largest engulfing circle to periapsis, and then adding on the area of the engulfing circle. The total area (for the entire flyby) is then double this quantity minus the imaged circle at periapsis, since the integral includes half of the periapsis circle. The difficulty lies in determining the value, θ_{0eng}, of θ_0 at which the engulfing condition, Equation (35), is met. An analytical solution has not been found for this quantity, necessitating a numerical solution. Two options are available for this, namely Equation (35) and Equation (25). The latitude ϕ of the envelope, given by the latter equation, is undefined when engulfing occurs, meaning that $\cos\phi > 1$. Due to gentler gradients, it is easier to solve $\cos\phi = 1$, than it is to solve Equation (35). A good initial guess for θ_{0eng} has been found to be the easily computed value of θ_0 when r is just less than r_f. Once θ_{0eng} has been found, ϕ_{0eng} can be easily found from Equation (18), and the area of the engulfing circle computed.

5.2. Verification of No Recounting

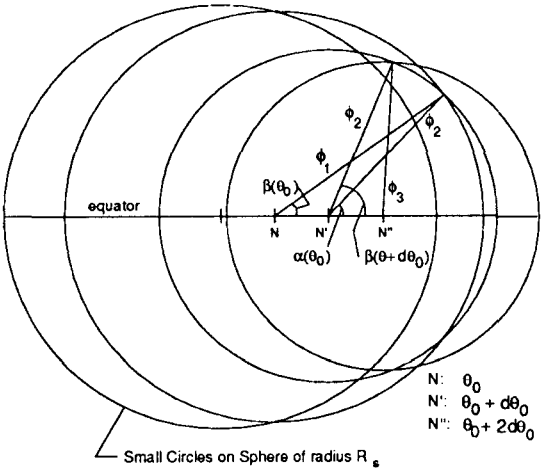

Fig. 9. A recounting scenario.

It has been assumed up to now that the crescent-shaped differential area segment was composed only of area previously unimaged. To see what conditions give rise to recounting, a hypothetical sequence of circles is shown in Figure 9, where the tips of the last crescent overlap with the second from the last crescent. Upon closer inspection, it is seen that the overlap shown will not occur if the value of $\beta(\theta_0 + d\theta_0)$ is less than the value of $\alpha(\theta_0)$. This is a sufficient condition, but not a necessary one, as overlap is also prevented by sufficiently increasing the size of only the leftmost circle, even though the stated condition is still met. Let $d\eta = \alpha(\theta_0) - \beta(\theta_0 + d\theta_0)$, and define a recount parameter, $\rho = d\eta/d\theta_0$. Then, $\rho > 0$ is a sufficient condition for no recounting. Taylor expansions similar to those performed earlier in this section yield

$$\rho = \frac{(1 - \phi_0'^2)\cos\phi_0 - \phi_0''\sin\phi_0}{\sqrt{1 - \phi_0'^2}\sin\phi_0}.$$

Although not shown here, the same condition holds for the $\phi_0' > 0$ case. As expected, this is not amenable to analytical integration. Numerically, all of the many examined cases of both E-limited and resolution limited viewing were found to give $\rho > 0$ for all true anomalies. This is not an unexpected result, however, since the instance of recounting shown in Figure 9 is highly contrived, in that ϕ_0 is not changing smoothly with θ_0. Thus, it is the belief of the authors that recounting will not pose a concern for these types of mapping. Moreover, numerical results using the area derivative equation agreed entirely with the results from direct integration under the envelope.

6. Imposition of a Terminator Condition and Camera Losses

Up to this point, no regard has been given as to whether the imaged area is illuminated by sunlight or not. Since most mapping instruments operate in the visible spectrum, this issue is an important one. A methodology is given below for computing the illuminated imaged area when the terminator lies along a meridian (otherwise the task is considerably more difficult). We first note that a meridional terminator condition in the cross-track case is trivially dealt with, since the terminator is parallel to the footprint.

As shown in Figure 10, θ_t denotes the longitude of a terminator, which crosses the envelope at point P. Opting to use the area derivative equation, we must first compute the true anomaly, θ_0, of the imaged circle which contributes the point P to the envelope. This must be done numerically from Equation (24). A good initial guess for θ_0, in the sense that the solution will most often converge, is found to be a value just below θ_{0eng} (to avoid the region where engulfing occurs), even though this may be far removed from the actual solution. Then the circle size is computed from Equation (18). Next Equation (34) is integrated from this circle to periapsis. Assuming westerly illumination, we compute

$$\text{Half-segment } PQS = \text{Sector } PNS - \triangle PNQ,$$

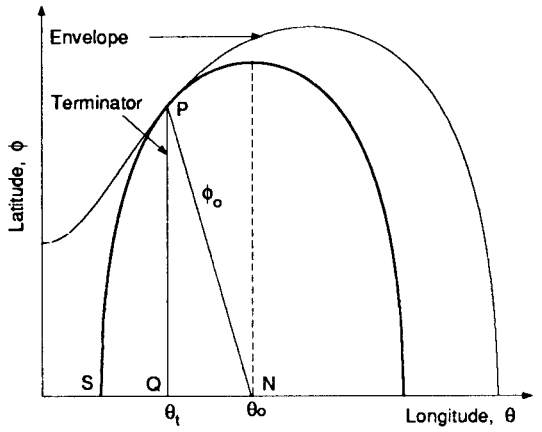

Fig. 10. Terminator geometry.

where the areas on the right can be easily computed from spherical geometry formulas, in a similar way to that shown in the derivation of Equation (34).

Camera losses will arise when the optics cannot adequately compensate for the spacecraft motion, a problem likely to occur near periapsis. A conservative estimate of the area imaged is found by discarding any scraps of area collected during camera loss time. The longitude at which camera losses commence can be treated exactly as a terminator, and the appropriate areas computed as above.

In the cross-track imaging case, the exact longitude at which camera losses commence is easily computed. Let the column width ε be defined as the difference in longitude between the easternmost and westernmost equatorial points of the scan column. Let τ_c be the time taken to scan one column. If contiguity of successive columns is required, then the time available for imaging one column is the time it takes for the nadir point of the spacecraft to move through a longitude equal to the column width. The spacecraft angular velocity is given by the conservation of angular momentum equation

$$\dot{\theta_0} = H/r^2.$$

Letting ω denote the angular rotation rate of the imaged body, and assuming the axis of rotation to be perpendicular to the orbital plane, then the time available is

$$t_a = \varepsilon/|\dot{\theta_0} - \omega| = \varepsilon r^2/|H - \omega r^2|.$$

Contiguous imaging is possible when

$$t_a \geq \tau_c.$$

The true anomaly at which contiguity ceases is obtained when equality holds in the above equation.

7. The Galileo Mission: A Numerical Example

By way of numerical example, the illuminated area mapped with conical imaging during one of Galileo's upcoming encounters with Callisto is computed as a function of flyby distance (r_p) for 1km and 80m resolution, and for various sun phase angles. In this example, the resolution limited theory is applied (and the Galileo project emission angle constraint of $E \leq 60°$ is ignored). The sun phase angle is defined as the longitude of the sun-pointing vector at closest approach, and it is assumed that the terminator is meridional and does not change position during the encounter. (Since Callisto rotates once every 17 days, this is a reasonable assumption for an encounter lasting only a few hours.) The following parameters were assumed for the encounter

$$R_s = 2445\text{km}\,, \quad v_\infty = 8\text{kms}^{-1}$$

$$\mu_s = 7172\text{km}^3\text{s}^{-2}\,, \; \delta = 0.02\text{mrad}$$

The trajectory in the vicinity of Callisto is approximated by a hyperbola. The asymptotic velocity, v_∞, of 8kms^{-1} is approximately the velocity Galileo will have in most of its encounters with Callisto. Through the conic and energy equations, the eccentricity is then given by $e = 1 + r_p R_s v_\infty^2/\mu_s$, where μ_s is the gravitational constant of Callisto. According to Wolf and Byrnes,[5] the periapsis radius of the closest encounter is planned to be 1.17 (2865km).

The imaged area is shown as a function of periapsis radius for various sun phase angles in Figures 11 and 12. As an aid in understanding the shapes of these graphs, Figures 13 and 14 show the corresponding envelopes obtained for selected values of periapsis radius. Certain features are apparent.

1. The envelopes shown in Figures 13 and 14 change from an igloo shape to a quarter-oval shape with increasing r_p.

2. Because of symmetry, the areas imaged at complementary sun phase angles will always add up to the total (light and dark) area that could be imaged.

3. For sun phase angles less than about 90°, the area first increases then decreases with r_p; while above about 90° the area decreases monotonically with r_p. This is because at appropriately small r_p (where the envelope at periapsis is close to the equator), a small increment in r_p sufficiently increases the area imaged at periapsis to overcome the area lost at the end of the envelope. Above a phase angle of about 90° this effect is negated because the area near periapsis is in darkness, and hence not imaged. The exact cut-off value of the phase angle depends on the

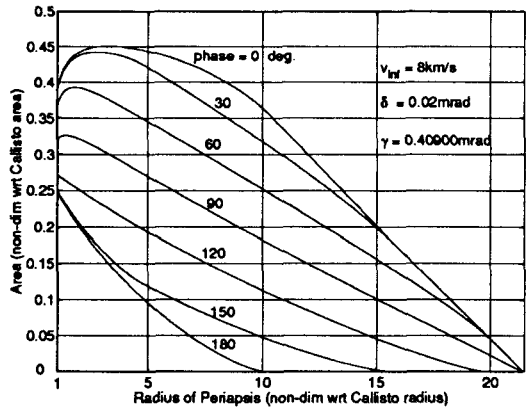

Fig. 11. Galileo coverage of Callisto with sun phase effects, 1km resolution.

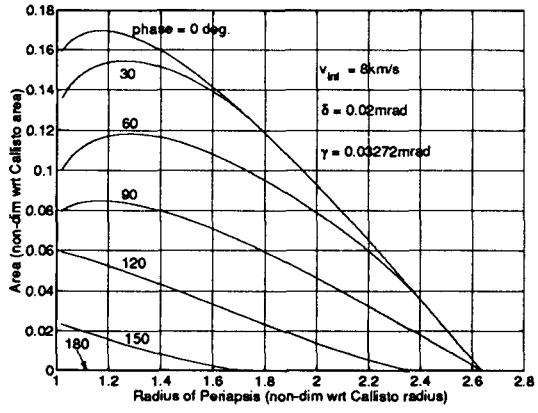

Fig. 12. Galileo coverage of Callisto with sun phase effects, 80m resolution.

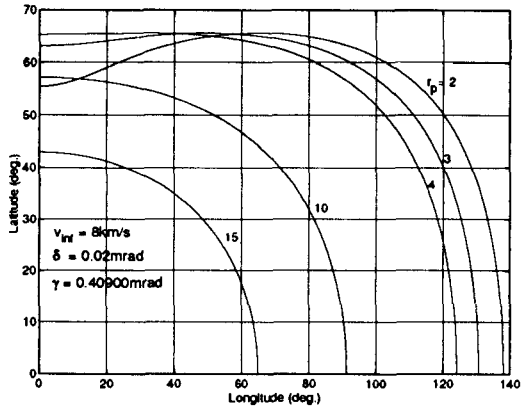

Fig. 13. Envelope curves on Callisto for various periapsis radii, 1km resolution.

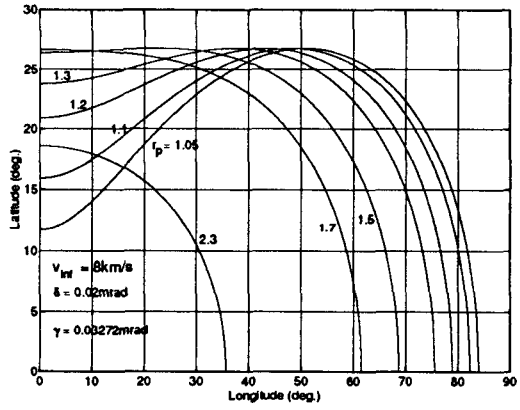

Fig. 14. Envelope curves on Callisto for various periapsis radii, 80m resolution.

imaging parameters chosen, but is expected to always lie somewhat above 90°.

4. For 80m resolution (Figure 12) the optimum r_p first increases and then decreases as the phase angle increases from zero. At phase zero, the optimum r_p is about 1.17; while at 30° the optimum is about 1.28. This is because the area gained at periapsis by the $r_p = 1.28$ envelope offsets the area it loses at the envelope ends, especially since the pre-periapsis end is in darkness and hence not imaged anyway (the terminator is at $-60°$ longitude). When the phase angle increases too much, however, the area lost (as r_p increases) at the illuminated envelope end is no longer offset by the area gained near periapsis. In contrast, for 1km resolution (Figure 11) the optimum r_p decreases monotonically with increasing phase angle. Around phase zero, the envelope ends are both in darkness, and at periapsis the envelope is at a higher latitude, thus disallowing the effects described above for the 80m resolution case.

5. In the 1km resolution case, the area curve for phase zero (Figure 11) shows a sudden change in slope just after $r_p = 10$ because the corresponding envelope (see Figure 13) meets the equator at ±90° longitude, exactly coinciding with the terminator. Similarly, a kink is seen in the 30° and 150° phase curves just after $r_p = 4$. However, since only one end of the envelope coincides with the terminator, the kink is not as sharp.

6. At 1km resolution the optimum r_p (at zero phase angle) is around 3.3 (8069km). For the 80m resolution case, the optimum r_p (at zero phase angle) is around 1.17 (2861km).

It is reemphasized here that items (1), (2), and (3) above are applicable to resolution limited conical viewing in general, and not just to the illustra-

tive case described here. Other mission scenarios can be analyzed and understood in a similar manner as above, providing mission designers a powerful tool in optimizing the mission's science return.

8. Conclusions

This paper provides an exact analysis of the coverage obtained under two imaging techniques—meridional cross-track scanning, and nadir-centered conical imaging—with two types of mapping requirements, namely viewing obliqueness (defined in terms of the emission angle) and resolution, applied to each. Not only does the analysis examine the actual magnitude of the imaged area, but also introduces envelope theory to obtain the boundary of the area imaged.

The magnitude of the imaged area is found exactly for the emission angle limited, cross-track scanning case. For the two conical imaging cases, an exact expression is found for the area acquisition rate with respect to the spacecraft true anomaly. This expression may be easily integrated numerically to obtain the total area. The cross-track, resolution limited area is also provided in terms of an integral that can be easily computed by quadrature. These should be invaluable aids to mission designers.

Several points relevant to the mission designer are illuminated by a numerical example. In the resolution limited, conical imaging case it is first noted that a closer flyby does not guarantee more area. Second, the optimum periapsis distance tends to decrease with stiffer resolution requirements (for a given optical system). Third, the optimum periapsis radius changes with sun phase angles less than slightly above 90°, while above this angle, the optimum is always unity (an impractical zero altitude periapsis). This paper also presents a simple and exact means for the designer to visualize the envelope of the imaged area.

Future work may include an analysis of the effects of the imaging parameters on the area, area-rate, and envelope equations, which could lead to the development of optimal solutions. It may also be feasible to develop approximations to the area-rate equation, possibly allowing an analytic integration to obtain the area. Additional work is also needed for an analytic understanding of the area graph characteristics. Lastly, and perhaps most importantly, the methods developed here could be applied to other imaging techniques, such as non-nadir centered conical imaging, in the hope of obtaining compact, easily computable expressions for the coverage obtained.

References

[1]Pease, C. B., *Satellite Imaging Instruments: Principles, Technologies and Operational Systems*, Ellis Horwood, New York, NY, 1991.

[2]Slater, P. N., *Remote Sensing: Optics and Optical Systems*, Addison-Wesley Publishing Company, Inc., Reading, MA, 1980.

[3]Longuski, J. M., and Myers, M. R., "Analytic Models of Mapping Coverage of the Galilean Satellites," AIAA Paper 84-1998, Aug. 1984.

[4]Boltyanskii, V. G., *Envelopes*, The MacMillan Co., New York, NY, 1964.

[5]Wolf, A. A., and Byrnes, D. V., "Design of the Galileo Satellite Tour," AAS Paper 93-567, Aug. 1993.